

Dataset Distillation with Probabilistic Latent Features

Zhe Li^{a,*}, Sarah Cechnicka^b, Cheng Ouyang^b, Katharina Breininger^a, Peter Schüffler^c, Bernhard Kainz^{a,b}

^a*IDEA lab, Friedrich Alexander Universität Erlangen-Nürnberg, Nürnberger Str. 74, Erlangen, 91052, Bayern, Germany*

^b*Imperial College London, 180 Queen's Gate, London, SW72AZ, , UK*

^c*Technical University Munich, Trogerstrasse 18, Munich, 81675, , Germany*

Abstract

As deep learning models grow in complexity and the volume of training data increases, reducing storage and computational costs becomes increasingly important. Dataset distillation addresses this challenge by synthesizing a compact set of synthetic data that can effectively replace the original dataset in downstream classification tasks. While existing methods typically rely on mapping data from pixel space to the latent space of a generative model, we propose a novel stochastic approach that models the joint distribution of latent features. This allows our method to better capture spatial structures and produce diverse synthetic samples, which benefits model training. Specifically, we introduce a low-rank multivariate normal distribution parameterized by a lightweight network. This design maintains low computational complexity and is compatible with various matching networks used in dataset distillation. After distillation, synthetic images are generated by feeding the learned latent features into a pretrained generator. These synthetic images are then used to train classification models, and performance is evaluated on real test set. We validate our method on several benchmarks, including ImageNet subsets, CIFAR-10, and the MedMNIST histopathological dataset. Our approach achieves state-of-the-art cross architecture performance across a range of backbone architectures, demonstrating its generality and effectiveness.

Keywords: Dataset Distillation, Stochastic Method, Image Classification

*Corresponding author

Email address: zhe.li@fau.de (Zhe Li)

1. Introduction

As data volumes continue to grow exponentially, training increasingly over-parameterized deep learning models incurs significant storage and computational costs. Dataset distillation addresses this challenge by synthesizing a compact set of representative images that encapsulates the essential characteristics of a larger dataset, enabling downstream tasks to achieve performance comparable to models trained on the full original dataset.

Early methods in dataset distillation primarily operated directly in the pixel space [1, 2, 3, 4, 5, 6], but these approaches often introduced noise and artifacts, especially in high-resolution images. Recent strategies, such as GLaD [7], have shifted attention to latent space distillation, leveraging pretrained generative models such as StyleGAN-XL [8] as deep generative priors. While latent space methods substantially reduce noise compared to pixel-space methods, they still struggle with residual artifacts due to insufficient consideration of spatial correlations and structural coherence within images.

In natural images, spatial correlation and structural coherence are fundamental, as neighboring pixels generally exhibit similar attributes and consistent semantic information. Existing distillation methods typically update images or latent representations through standard backpropagation without explicitly modeling these spatial relationships. Such an approach neglects the inherent ambiguity of the dataset distillation process, where multiple valid synthetic representations might exist. Effectively modeling this inherent uncertainty could significantly improve the distillation outcomes by guiding synthetic image generation toward structurally consistent and semantically meaningful results. Uncertainty in image data typically comprises aleatoric uncertainty, which stems from inherent variability in the observations, and epistemic uncertainty, arising from incomplete knowledge or limited data [9]. Specifically, aleatoric uncertainty in images is often spatially correlated and exhibits heteroscedasticity, reflecting varied uncertainty across different regions within the same image [10]. However, pretrained generative models like StyleGAN-XL typically produce deterministic and spatially independent outputs, limiting their ability to fully capture structured uncertainty.

To address this limitation, we introduce the Stochastic Latent Feature Distillation (SLFD) framework. SLFD explicitly models spatial correlations

and uncertainty within latent features by employing a low-rank multivariate normal distribution. Given that synthetic images are ultimately produced from latent features passed through a pretrained generator, we assume that directly modeling uncertainty within the latent feature space provides an efficient and effective approach. The stochastic component of our method generates multiple latent feature samples, explicitly embedding spatial coherence and uncertainty into the distillation process. Additionally, our proposed module is compact and comprises only three linear layers, ensuring compatibility with existing matching algorithms without necessitating architectural modifications.

Beyond natural image datasets, dataset distillation is increasingly valuable in healthcare settings, where data privacy and efficient data sharing are critical [11, 12, 13]. Synthesizing anonymized and compact representations can facilitate secure data sharing among clinical institutions by effectively removing identifiable patient information. In our experiments, we demonstrate the effectiveness of SLFD on histopathological image datasets, highlighting its potential for impactful applications in medical imaging.

Our contributions can be summarized as follows:

1. We introduce Stochastic Latent Feature Distillation (SLFD), a novel dataset distillation framework that incorporates structured uncertainty through a low-rank multivariate distribution, enabling the generation of informative and spatially coherent synthetic data.
2. SLFD effectively models spatial relationships in the latent space and maintains high performance even at large image resolutions, offering robustness and scalability with minimal computational overhead.
3. Through extensive experiments on CIFAR-10 and multiple ImageNet subsets, SLFD outperforms state-of-the-art methods across diverse architectures, demonstrating strong cross-model generalization.
4. We validate SLFD on the MedMNIST histopathology dataset, where it shows consistent quantitative improvements and clear qualitative distinctions, proving its adaptability to complex real-world domains.

2. Related work

2.1. Dataset distillation

A comprehensive overview over dataset distillation is provided in recent surveys [14, 15]. After the pioneered [16], efficiency has been addressed by

Generative Teaching Networks (GTNs) [17] and through model regularization techniques [18]. The field diversified into various matching methods to align the original and the synthesized data, such as Dataset Condensation with Gradient Matching (DC) [1, 2, 5], Distribution Matching (DM) [4, 6], and Matching Training Trajectories (MTT) [3]. Beyond matching strategies, methods to align features of convolutional networks [19, 20] have been proposed to improve performance. [21] enhanced the correlation between generated samples through factorization during training. [22] tackled the challenge of accumulated trajectory errors in weight initialization during the evaluation phase by guided flat trajectories during training. [23] introduced new calibration techniques for deep neural networks to mitigate overconfidence issues and the over-concentration in distillation data.

Recognizing the limitations of pixel space, characterized by high-frequency noise, [24] shifted focus to synthesizing images in the latent space using pre-trained GANs, thereby extracting more informative samples. Aiming for simplicity and efficiency, [7] utilized a pre-trained StyleGAN-XL [8] to create a single synthetic image per class from latent space, streamlining the distillation process from real datasets. The field continues to evolve with methods addressing various phases of dataset distillation, including the introduction of the distillation space concept [25] and the implementation of a clustering process for selecting mini-batch real images [26].

2.2. Stochastic mapping

Bayesian methods have experienced significant attention for neural network robustness, uncertainty estimation, and model regularization. In classification, significant efforts focus on predicting Dirichlet distributions [27, 28, 29] and post-training calibration of predicted class probabilities [30]. Other approaches [31] and effective approximations [10] have highlighted the importance of well-calibrated uncertainty estimates in deep neural networks, especially in applications like medical diagnosis, where decision-making under uncertainty is crucial.

2.3. Medical applications

For medical images, dataset distillation is attractive from a privacy and data sharing perspective. For histopathology images, [32] works on MedMnist dataset by a community detection method. For other medical datasets, the fundamental dataset distillation framework has been applied on gastric X-ray images [33, 34] and a COVID-19 chest X-ray dataset [35].

3. Method

This section introduces the proposed Stochastic Latent Feature Distillation (SLFD) framework, with an overview provided in Fig.2. To offer an intuitive understanding of the approach, Fig.1 illustrates a simplified example involving two pixels within a probabilistic graphical model, highlighting the role of uncertainty and spatial correlation. The core of SLFD is a lightweight stochastic module (Fig.2(b)), described in detail in Section3.2. This module learns a structured distribution over latent features, enabling the generation of diverse and spatially consistent synthetic samples during the distillation process. Section 3.3 and Fig. 2(c) explain how we define a stochastic loss function that incorporates samples from the learned latent distribution. This loss guides the optimization process to produce synthetic data that more faithfully preserves the structure and variability of the original dataset. Finally, as shown in Fig. 2(d), we assess the quality of the distilled dataset by training independent classifiers solely on the synthetic images.



Figure 1: Probabilistic graphical model for a two-pixel sample synthesis problem. Circular shapes indicate random variables, while diamond shapes represent deterministic variables. Variables that are shaded represent observed data, whereas those that are unshaded are unobserved. \mathbf{x} are pixels of the synthesized image, \mathbf{y} are the class labels, $\boldsymbol{\eta}$ are latent features, $f_\phi(\boldsymbol{\eta})$ indicates an implicit latent variable model, where f_ϕ can be a GAN’s generator. GAN discriminators are omitted as auxiliary objects that approximate an f-divergence. Note that our approach assumes $\boldsymbol{\eta}$ to be probabilistic and dependent in contrast to previous work [7]. We hypothesize that this allows to capture spatial correlations in latent space during the distillation phase.

3.1. Preliminaries

3.1.1. Problem introduction

Dataset distillation is a process where the information contained within a large real dataset \mathcal{T} is ideally condensed into a significantly smaller synthetic dataset \mathcal{S} . Formally, given a real dataset $\mathcal{T} = \{(x_i, y_i)\}_{i=1}^N$, where $x_i \in$

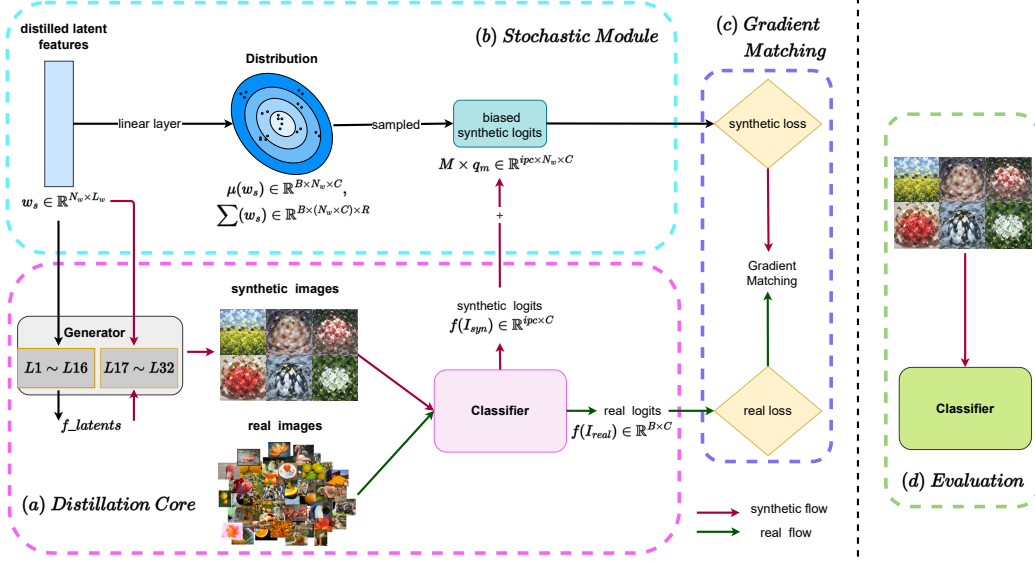


Figure 2: Overview of the proposed SLFD framework. (a) The distillation backbone is based on GLaD [7], where the generator (shown in gray to indicate frozen weights) is split into two parts: the first 16 layers compute intermediate features f_n from latent codes w_s (black arrows), and the remaining 16 layers generate synthetic images using both w_s and f_n (red arrows). (b) The Stochastic Module models uncertainty in the latent space by estimating a low-rank multivariate normal distribution using three linear layers to compute the mean, variance, and covariance factors. Multiple samples drawn from this distribution are used to represent synthetic probability distributions. (c) The Gradient Matching component computes the matching loss between gradients of real and synthetic data. (d) In the Evaluation phase, classifiers are trained solely on the distilled synthetic images.

$\mathbb{R}^{3 \times H \times W}$ denotes an image, $y_i \in \{0, 1, 2, \dots, C\}$ represents its corresponding class label, in a dataset with C total classes and N total samples. Our task is to synthesize a small synthetic dataset $\mathcal{S} = \{(s_i, y_i)\}_{i=1}^{N_s}$, where $N_s = ipc \times C$, ipc denotes images per class, and $N_s \ll N$. In our experiments, *e.g.*, $ipc = 1$ means there is only one image synthesized for each class.

3.1.2. Distillation core

To mitigate the noise and visual artifacts often introduced by pixel-level distillation methods, GLaD [7] performs dataset distillation in the latent space using a pretrained generator as a prior, as illustrated in Fig. 2(a). At the beginning of training, latent codes $z_s \in \mathbb{R}^{B \times L_z}$ are sampled from a standard normal distribution $\mathcal{N}(0, 1)$. These codes are then projected into the

extended latent space W^+ [36] to produce latent features $w_s \in \mathbb{R}^{B \times N_w \times L_w}$, where N_w denotes the number of style blocks in the StyleGAN-XL mapping network and L_w is the dimensionality of each feature vector. To enrich the representation and encourage diversity in the synthetic images, the method also extracts intermediate feature activations f_n from a selected hidden layer n within the generator. These features, referred to as F_n , provide additional context and structure when synthesizing images. During the distillation process, synthetic images are generated by passing both w_s and f_n through the latter layers of the frozen StyleGAN-XL generator. The training objective involves matching gradients between synthetic and real images to preserve semantic alignment. After distillation, the quality of the synthetic dataset is evaluated by training classifiers solely on these generated images, and performance is measured using test accuracy on a real validation set.

3.2. Stochastic training

The motivation for integrating the stochastic module into the distillation framework is to incorporate structured uncertainty into the image generation process, which is typically absent in deterministic models. Inspired by [10], we observe that both the generator and classifier in conventional distillation pipelines behave as deterministic functions. As a result, the synthetic image outputs are treated as independent across pixels, overlooking the spatial dependencies inherent in natural images. To address this, we propose modeling the distribution over the classifier outputs for synthetic images using a multivariate normal distribution:

$$f(I_{\text{syn}}) \mid S \sim \mathcal{N}(\mu(S), \Sigma(S)) \quad (1)$$

Since these synthetic images are generated from latent features, we redefine the distribution in terms of the generator:

$$f(I_{\text{syn}}) \mid G_{16}(w_s; G_0(w_s)) \sim \mathcal{N}(\mu(w_s), \Sigma(w_s)) \quad (2)$$

where w_s is the latent input, $G_0(w_s)$ produces intermediate features f_n from the first part of the generator, and G_{16} refers to the second half of the generator that produces the image. Here, $\mu(w_s) \in \mathbb{R}^{B \times N_w \times C}$ is the mean vector, and $\Sigma(w_s) \in \mathbb{R}^{B \times (N_w \times C)^2}$ is the full covariance matrix. The output dimension C corresponds to the number of classes predicted by the classifier, replacing the latent feature dimensionality L_w . We use a batch size B equal to C , following the convention of one synthetic image per class.

Algorithm 1 Our proposed SLFD approach.

Input: The generator G , Real dataset \mathcal{T} , C , $Epoch$, and batch size B .
Initialize latent features w_s and f_n and the Stochastic Module .
for epoch from 0 to $Epoch$ **do**
 Synthetic images $\mathcal{S} = G(w_s, f_n)$; Initialize the distillation model f .
 for each class c in C **do**
 $I_{real}^c \sim \text{RandomSubset}(\mathcal{T}_c, B) \rightarrow f(I_{real}^c) \rightarrow \mathcal{L}_{real}^c$
 $I_{syn}^c \subset \mathcal{S} \rightarrow f(I_{syn}^c) \rightarrow \{\mu(w_s), \Sigma(w_s)\} \rightarrow \{q_m\}_{m=1}^M$
 Update $q_m^* = q_m - \mu(w_s) + f(I_{syn}^c)$
 Calculate \mathcal{L}_{syn}^c
 Calculate gradient matching loss $\mathcal{L} = 1 - \frac{\nabla_{\theta} \mathcal{L}_{syn}^c \cdot \nabla_{\theta} \mathcal{L}_{real}^c}{\|\nabla_{\theta} \mathcal{L}_{syn}^c\| \|\nabla_{\theta} \mathcal{L}_{real}^c\|}$
 end for
 Update the latent features w_s and f_n by backpropagation.
end for Distillation
Synthetic images $\mathcal{S} = G(w_s, f_n)$.
Train five models only on the $ipc \times C$ synthetic images S .
Evaluate all models on large real test set.

To manage computational complexity, we approximate the full covariance with a low-rank formulation:

$$\Sigma = PP^T + D \quad (3)$$

where $P \in \mathbb{R}^{B \times (N_w \times C) \times R}$ is the low-rank covariance factor, R is the rank, and $D \in \mathbb{R}^{B \times N_w \times C}$ is the covariance diagonal. Each parameter of the distribution, including the mean, covariance diagonal, and covariance factor, is predicted by an individual fully connected layer. The resulting distribution is cached and used to sample multiple latent representations during training. These samples serve as stochastic predictions, contributing to the loss calculation. As training progresses, latent features are updated iteratively, and their associated distributions are refreshed accordingly, as described in Algorithm 1.

3.3. Loss function

3.3.1. Stochastic loss

To enhance the training process with uncertainty modeling, we define a stochastic loss over the classifier outputs for synthetic images. In total,

we generate $\text{ipc} \times C$ synthetic images using both latent features w_s and intermediate features f_n from the pretrained StyleGAN-XL generator.

After computing the loss on a batch of real images, we calculate the corresponding loss \mathcal{L}_{syn} for the synthetic images of the same class using a probabilistic sampling approach. Specifically, the synthetic images are passed through the same classifier as the real ones to produce output probabilities $f(I_{\text{syn}})$. To incorporate stochasticity, we approximate the negative log-likelihood using Monte Carlo integration:

$$\begin{aligned} -\log p(y \mid x) &= -\log \int p(y \mid f(I_{\text{syn}})) p(f(I_{\text{syn}}) \mid x) df(I_{\text{syn}}) \\ &\approx -\log \frac{1}{M} \sum_{m=1}^M p(y \mid f(I_{\text{syn}})_m) \end{aligned} \quad (4)$$

For simplicity, we define each sample $f(I_{\text{syn}})_m$ as q_m , where $q_m \mid w_s \sim \mathcal{N}(\mu(w_s), \Sigma(w_s))$, based on the latent feature distribution described in Section 3.2. We sample M such instances, $\mathcal{Q} = \{q_m \in \mathbb{R}^{\text{ipc} \times N_w \times C}\}_{m=1}^M$. Since the classifier outputs $f(I_{\text{syn}}) \in \mathbb{R}^{\text{ipc} \times C}$ also carry meaningful semantic information, we combine them with the sampled predictions to construct refined probability estimates. The refined probabilities are computed by shifting each sample by the classifier’s output:

$$q_m^* = q_m - \mu(w_s) + f(I_{\text{syn}}) \quad (5)$$

This step adjusts each sample to reflect both the stochastic variability from the latent space and the semantic grounding from the classifier as in Fig. 3. The intuition is that the sampled probabilities encode spatial structure, while the classifier output mitigates uncertainty introduced during generation, especially at high resolutions. We then compute a cross-entropy-based loss between these adjusted samples and the true class labels:

$$\mathcal{L}_{\text{syn}}^c = -\frac{1}{N_w \times M} \sum_{w=1}^{N_w} \sum_{m=1}^M \left(\log \sum_{c=1}^M \exp(y_c \cdot (q_m^*)_c) + \log M \right) \quad (6)$$

Here, the label y_c is repeated M times to match the number of samples. As in prior work [10], we apply the log-sum-exp trick for numerical stability.

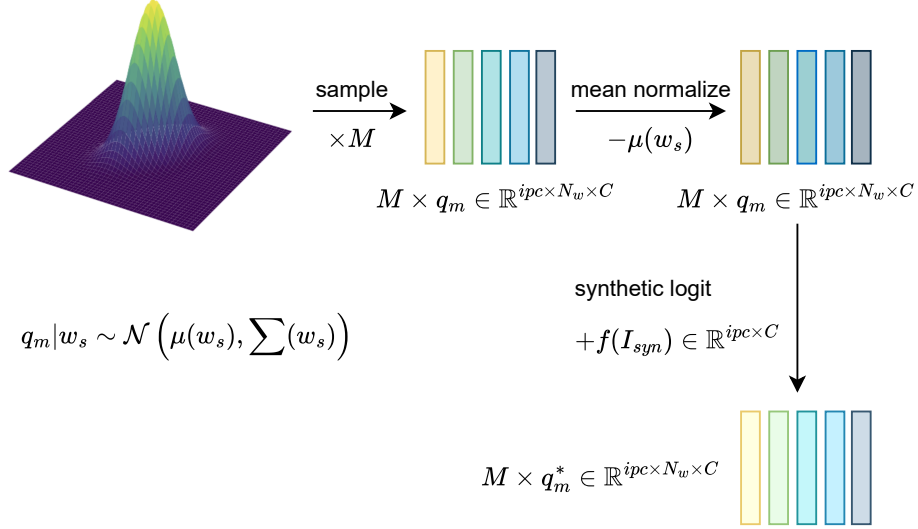


Figure 3: Illustration Eq. 5 about how we sample probabilities.

3.3.2. Gradient matching loss

To further align synthetic data with the underlying distribution of real data, we apply gradient matching during distillation. Each class is processed independently. For real images, we compute the standard cross-entropy loss, denoted $\mathcal{L}_{\text{real}}^c$, based on the classifier’s predictions and the ground truth labels. We then explicitly compute the gradients of $\mathcal{L}_{\text{real}}^c$ and the stochastic loss $\mathcal{L}_{\text{syn}}^c$ with respect to the classifier parameters. This new gradient matching loss ensures that the synthetic data not only reflect class semantics but also induce training dynamics consistent with those of the original dataset.

4. Experiments

4.1. Datasets and metrics

We evaluate our distillation framework on three benchmark datasets: ImageNet-1K [37], CIFAR-10 [38], and MedMNIST [39], covering both natural and medical imaging domains. For ImageNet-1K, we conduct experiments on two configurations: 10 class-balanced subsets at a resolution of 128×128 , and 5 subsets at a higher resolution of 256×256 . Each subset contains 10 classes which have similar categories. CIFAR-10 is a standard benchmark

for low-resolution image classification, consisting of 60,000 images (6,000 per class) across 10 categories, each image having a resolution of 32×32 .

For the medical domain, we use the PathMNIST variant of the MedMNIST collection [39], which focuses on histopathology images. This dataset contains a total of 107,180 samples, split into 89,996 for training, 10,004 for validation, and 7,180 for testing. All images are resized to 28×28 to standardize input dimensions.

To benchmark our approach, we compare against recent state-of-the-art methods such as GLaD [7], focusing on the downstream classification task. We report the cross-architecture test accuracy to assess generalization and robustness of the distilled datasets.

4.2. Implementation details

The distillation process is performed using a ConvNet architecture. Once the synthetic dataset is generated, we evaluate its effectiveness by training 5 different classifiers, ConvNet, ResNet18, VGG11, ViT, and AlexNet, on the distilled images. These models are then tested on the real validation sets from ImageNet in all experimental settings. Our primary evaluation metric is cross-architecture accuracy, which reflects the average test performance of the 4 classifiers not involved in distillation (ResNet18, VGG11, ViT, and AlexNet). This setup is intended to assess the generalization ability of the distilled data across different model architectures. For completeness, we also report results when the ConvNet is used for both distillation and downstream classification. Each reported accuracy is averaged over 5 independent runs, and we include the corresponding standard deviation to reflect consistency and reliability. All experiments are conducted on a single NVIDIA A100 GPU. The total runtime is approximately 9 hours, which includes the full distillation process, training, and evaluation of all 5 classifiers at every 100 iterations across 5 repetition runs. This computational setup is comparable to that used in GLaD.

4.3. Benchmark dataset results

4.3.1. ImageNet

Table 1 presents a comparison between our method and existing state-of-the-art techniques across 10 subsets of the ImageNet dataset at a resolution of 128×128 . Our approach shows consistent improvements in cross-architecture performance, achieving up to a 7% gain when using gradient matching (DC) and up to 36% with distribution matching (DM). The ConvNet classifier,

	methods	ImNet-A	ImNet-B	ImNet-C	ImNet-D	ImNet-E	ImNette	ImWoof	ImNet-Birds	ImNet-Fruits	ImNet-Cats
MTT [3]	pixel	33.4 \pm 1.5	34.0 \pm 3.4	31.4 \pm 3.4	27.7 \pm 2.7	24.9 \pm 1.8	24.1 \pm 1.8	16.0 \pm 1.2	25.5 \pm 3.0	18.3 \pm 2.3	18.7 \pm 1.5
	GLaD [7]	39.9 \pm 1.2	39.4 \pm 1.3	34.9 \pm 1.1	30.4 \pm 1.5	29.0 \pm 1.1	30.4 \pm 1.5	17.1 \pm 1.1	28.2 \pm 1.1	21.1 \pm 1.2	19.6 \pm 1.2
DC [1]	pixel	38.7 \pm 4.2	38.7 \pm 1.0	33.3 \pm 1.9	26.4 \pm 1.1	27.4 \pm 0.9	28.2 \pm 1.4	17.4 \pm 1.2	28.5 \pm 1.4	20.4 \pm 1.5	19.8 \pm 0.9
	GLaD [7]	41.8 \pm 1.7	42.1 \pm 1.2	35.8 \pm 1.4	28.0 \pm 0.8	29.3 \pm 1.3	31.0 \pm 1.6	17.8 \pm 1.1	29.1 \pm 1.0	22.3 \pm 1.6	21.2 \pm 1.4
	SLFD	43.27\pm1.58	43.31\pm1.13	36.76\pm1.10	29.26\pm1.46	31.02\pm1.40	33.10\pm1.18	19.13\pm1.05	30.22\pm1.22	23.62\pm1.26	21.65\pm1.30
	GLaD-Conv	44.1 \pm 2.4	49.2 \pm 1.1	42.0 \pm 0.6	35.6 \pm 0.9	35.8\pm0.9	35.4 \pm 1.2	22.3 \pm 1.1	33.8 \pm 0.9	20.7 \pm 1.1	22.6 \pm 0.8
	SLFD-Conv	46.00\pm1.39	49.96\pm0.97	42.60\pm1.00	36.40\pm2.26	35.44 \pm 0.60	36.72\pm1.31	22.68\pm0.92	33.88\pm1.01	21.96\pm0.45	24.12\pm1.03
DM [4]	pixel	27.2 \pm 1.2	24.4 \pm 1.1	23.0 \pm 1.4	18.4 \pm 1.7	17.7 \pm 0.9	20.6 \pm 0.7	14.5 \pm 0.9	17.8 \pm 0.8	14.5 \pm 1.1	14.0 \pm 1.1
	GLaD [7]	31.6 \pm 1.4	31.3 \pm 3.9	26.9 \pm 1.2	21.5 \pm 1.0	20.4 \pm 0.8	21.9 \pm 1.1	15.2 \pm 0.9	18.2 \pm 1.0	20.4 \pm 1.6	16.1 \pm 0.7
	SLFD	39.18\pm1.57	38.30\pm1.08	32.02\pm2.30	25.21\pm2.10	23.52\pm1.73	28.67\pm1.00	17.53\pm1.03	24.70\pm2.55	23.25\pm1.54	18.37\pm0.71
	GLaD-Conv	41.0 \pm 1.5	42.9 \pm 1.9	39.4 \pm 0.7	33.2 \pm 1.4	30.3 \pm 1.3	32.2 \pm 1.7	21.2 \pm 1.5	27.6 \pm 1.9	21.8 \pm 1.8	22.3 \pm 1.6
	SLFD-Conv	58.72\pm1.50	54.04\pm1.13	46.56\pm1.66	41.88\pm1.09	37.68\pm0.70	43.72\pm0.92	25.44\pm1.57	38.08\pm0.92	35.44\pm0.72	27.56\pm0.77

Table 1: Cross architecture test accuracy on ImageNet with resolution 128×128 . We distill 1 synthetic image for each class by ConvNet and train all 5 classifiers on these 10 synthetic images for each subset. We report the average results of 4 unseen classifiers, ResNet18, VGG11, ViT, and AlexNet, on a real validation set to improve generalization. The rows with ”*-Conv” are the results of ConvNet.

	ImNet-A	ImNet-B	ImNet-C	ImNet-D	ImNet-E
DC [1]	38.3 \pm 4.7	32.8 \pm 4.1	27.6 \pm 3.3	25.5 \pm 1.2	23.5 \pm 2.4
GLaD [7]	37.4 \pm 5.5	41.5 \pm 1.2	35.7 \pm 4.0	27.9 \pm 1.0	29.3 \pm 1.2
SLFD	44.01\pm1.68	43.15\pm1.64	37.28\pm1.38	29.78\pm1.07	31.57\pm0.99

Table 2: Cross architecture test accuracy on 5 subsets of ImageNet (256×256) with DC method.

which is also used during distillation, achieves performance gains of up to 7% and 63%, particularly notable on the ImNet-Fruits subset. In Table 2, we report results on 5 subsets at a higher resolution of 256×256 . Across all subsets, SLFD improves classification accuracy, with the ImNet-A subset showing a significant boost of 17.7%. Importantly, no performance degradation is observed with the increased resolution, highlighting the robustness and scalability of our method.

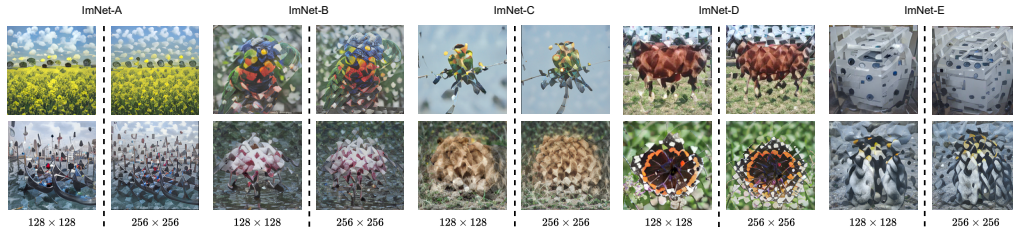


Figure 4: Example images distilled from ImageNet subsets.

	average	AlexNet	ResNet18	VGG11	ViT
SLFD (50)	14.28 \pm 0.91	12.60 \pm 1.41	11.02 \pm 0.91	17.25 \pm 0.64	16.23 \pm 0.70
SLFD (100)	7.47 \pm 0.37	6.64 \pm 0.36	4.18 \pm 0.33	9.24 \pm 0.42	9.81 \pm 0.35

Table 3: Cross architecture results with more classes (in brackets) with DC.

Figure 4 presents qualitative results of synthetic images generated by our SLFD method. These samples can be broadly divided into two categories. In the first row, the synthetic images closely reflect recognizable features from the corresponding real-world classes, capturing salient visual cues that align with human interpretation. In contrast, the second row contains examples where object-level clarity is reduced. These images often contain overlapping parts or fragmented features, for instance, multiple boats appearing merged in the *Gondola* class or compressed wing patterns in the *Admiral* butterfly category. Although individual objects may be harder to distinguish, higher-resolution synthesis contributes to richer visual content, revealing finer details or a greater density of object-related elements. It is important to note that generating photorealistic images is not the primary goal of dataset distillation. Instead, the objective is to encode class-discriminative features that facilitate effective model training. While some synthetic images may appear ambiguous or unintelligible to human observers, they can still provide meaningful training signals. Often, these images prioritize texture and statistical patterns over explicit structure, especially when classes within a subset share visual similarities. This is consistent with findings in prior work [3], where the utility of synthetic data lies more in its representational efficiency than in its visual fidelity.

To further evaluate the scalability and generalization of our method, we extend our experiments beyond individual subsets. Specifically, we combine 5 subsets (ImNet-A through ImNet-E), each with a resolution of 128×128 , to form a new dataset comprising 50 classes. Additionally, we merge all 10 subsets to create a 100-class configuration. The cross-architecture performance of our method on these larger and more diverse datasets is reported in Table 3, where we evaluate using four classifiers that were not involved in the distillation process.

	average	AlexNet	ResNet18	VGG11	ViT
pixel	26.0 \pm 0.4	25.9 \pm 0.2	27.3 \pm 0.5	28.0 \pm 0.5	22.9 \pm 0.3
GLaD G_r [7]	26.6 \pm 0.6	30.1\pm0.5	27.3 \pm 0.2	28.0 \pm 0.9	21.2 \pm 0.6
GLaD G_t [7]	26.3 \pm 0.5	26.0 \pm 0.7	27.6 \pm 0.6	28.2 \pm 0.6	23.4 \pm 0.2
SLFD G_t	28.1\pm0.55	26.79 \pm 0.55	28.45\pm0.94	28.73\pm0.38	28.45\pm0.33

Table 4: Cross architecture results on CIFAR-10 with DC and random initialization G_r or pre-trained G_t .

4.3.2. CIFAR-10

Following our evaluation on ImageNet, we assess the effectiveness of SLFD on the CIFAR-10 dataset to test its generalization to lower-resolution data. Table 4 reports results across 4 classifiers not used during distillation. We consider two generator settings: G_r , where the generator is randomly initialized, and G_t , where the generator is pretrained on the ImageNet dataset. Across both settings, our method consistently outperforms GLaD [7], demonstrating the adaptability of SLFD to different data domains and resolutions.

4.3.3. MedMNIST

Building on our results from natural image datasets, we further evaluate SLFD on the MedMNIST dataset to test its effectiveness in the medical imaging domain. Table 5 presents the classification performance across various input resolutions. For training, we upsample the original 28×28 images to resolutions of 64, 128, and 256 using bicubic interpolation. While the performance of GLaD [7] slightly declines as image resolution increases from 64 to 256, our method shows a consistent improvement, demonstrating greater robustness and suitability for high-resolution medical imagery. Figure 5 provides qualitative examples of the generated synthetic data. The 9 classes in the dataset are visually distinguishable, indicating that SLFD effectively captures class-specific structure. Notably, the real histology images predominantly appear in shades of pink due to hematoxylin and eosin (H&E) staining. In contrast, our synthetic images exhibit a broader color range, including green and light blue, resulting from normalization applied during preprocessing. This variation does not hinder classification, suggesting that our method can retain discriminative features even under color shifts.

	res=64	res=128	res=256
GLaD [7]	36.88 \pm 1.14	35.77 \pm 1.23	35.64 \pm 1.68
SLFD	36.67 \pm 0.61	36.27 \pm 1.70	37.17 \pm 2.27

Table 5: Cross architecture result on MedMNIST [39].

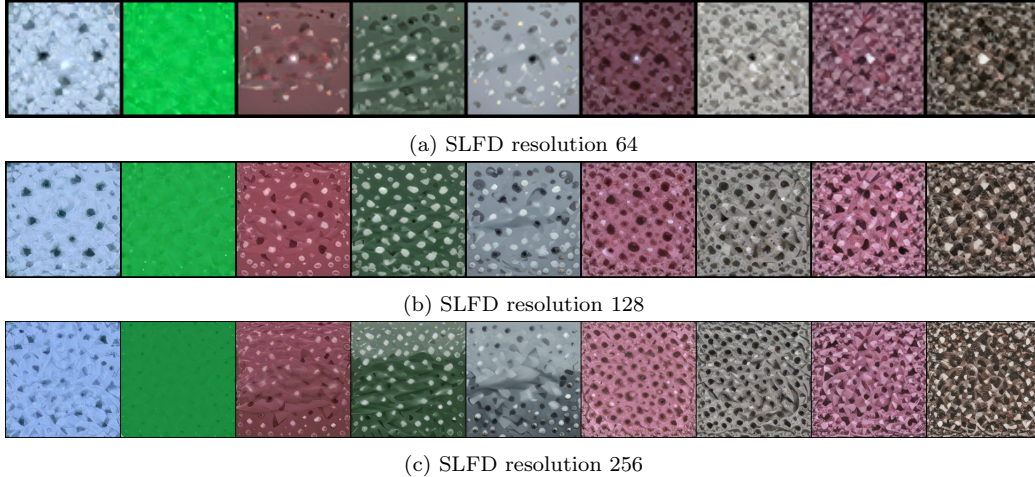


Figure 5: Synthetic images from MedMNIST [39] for different output resolutions.

4.4. Ablation study

To better understand the impact of the generative backbone, we compare two generative models: StyleGAN-XL and the class-conditional diffusion model UViT [40]. The results are summarized in Table 6. In this experiment, we integrate UViT into our distillation pipeline by replacing StyleGAN-XL with UViT as the generator. To simplify the integration, we exclude the autoencoder component of the diffusion model and adapt the remaining modules to our framework. Since UViT expects two-dimensional latent inputs, we reshape our existing 1D latent representations into a 32×32 spatial format. After training, we use both w_s and f_n to generate synthetic images through UViT. All other experimental configurations are kept consistent to ensure a fair comparison. The results show that UViT underperforms compared to StyleGAN-XL in this setting. We attribute this to the fact that the latent features generated by the mapping network are specifically structured for the StyleGAN-XL architecture, and may not transfer effectively to a diffusion-based generator. Figure 6 shows qualitative examples of syn-

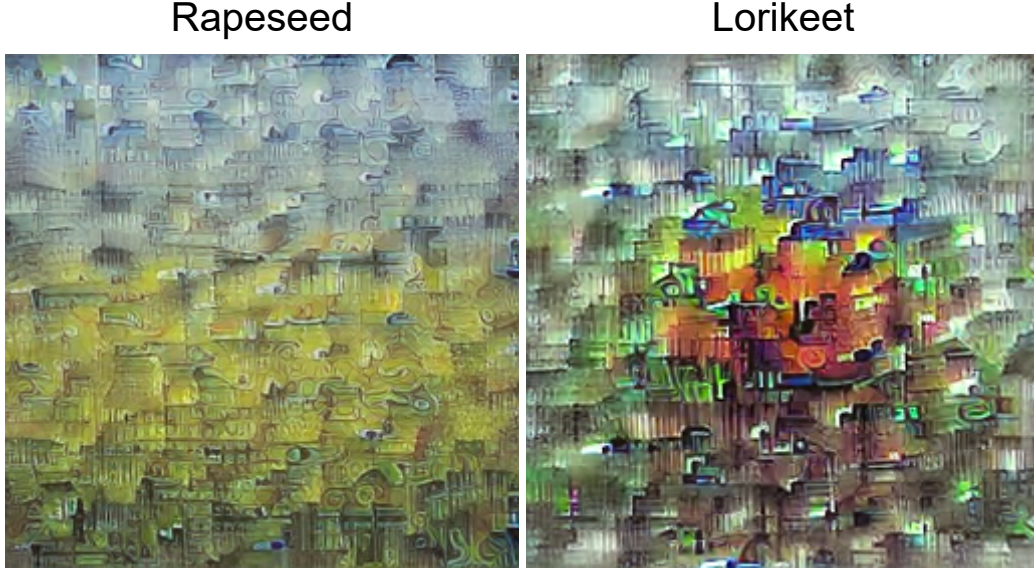


Figure 6: Results of ablation study. Distilled images with the diffusion model UViT [40] with resolution (256×256) .

thetic images generated using UViT. Notably, these images emphasize global structure, which aligns with the inductive bias of vision transformers [41].

We further evaluate the effectiveness of our low-rank multivariate normal approximation by comparing it to a full-rank variant. As shown in Table 7, our low-rank formulation achieves performance that is on par with, or in some cases exceeds, that of the full-rank counterpart across 5 ImageNet subsets. This indicates that the low-rank approximation retains sufficient expressiveness to generate informative synthetic images while offering improved computational efficiency. Qualitative results are presented in Fig. 7.

	Methods	ImNet-A	ImNet-B	ImNet-C	ImNet-D	ImNet-E
GAN	GLaD	$37.4_{\pm 5.5}$	$41.5_{\pm 1.2}$	$35.7_{\pm 4.0}$	$27.9_{\pm 1.0}$	$29.3_{\pm 1.2}$
	SLFD	$44.01_{\pm 1.68}$	$43.15_{\pm 1.64}$	$37.28_{\pm 1.38}$	$29.78_{\pm 1.07}$	$31.57_{\pm 0.99}$
UViT	GLaD	$37.70_{\pm 1.53}$	$38.96_{\pm 1.68}$	$33.11_{\pm 1.65}$	$26.38_{\pm 1.24}$	$27.34_{\pm 1.11}$
	SLFD	$37.92_{\pm 2.11}$	$38.97_{\pm 1.82}$	$32.67_{\pm 1.50}$	$26.78_{\pm 1.28}$	$28.21_{\pm 1.62}$

Table 6: GAN vs. UViT [40] as backbone for f_n , pretrained on ImageNet.

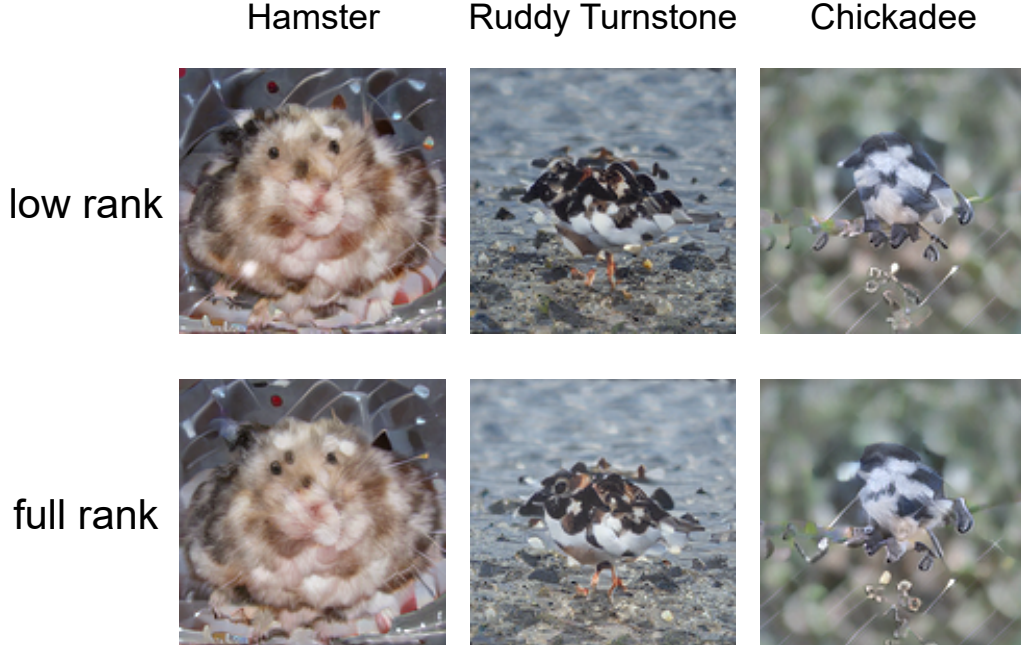


Figure 7: Results of ablation study. Qualitative examples from low-rank SLFD and full-rank SLFD on ImageNet with resolution (128×128).

In some cases, such as the *Hamster* class, synthetic samples appear visually similar and are difficult to distinguish, regardless of the covariance rank. The full-rank version occasionally captures finer details, for example, the eye of the *Ruddy Turnstone* is more pronounced. However, the low-rank approximation also shows advantages in certain instances, such as more defined mouth features in the *Chickadee* class. These results demonstrate that the low-rank strategy maintains a strong balance between efficiency and image quality. Notably, this observation holds even at higher resolutions, such as 256×256 , where detail preservation is typically more challenging.

5. Conclusion

In this work, we propose Stochastic Latent Feature Distillation (SLFD), a novel framework for dataset distillation that explicitly models spatial correlations through a low-rank multivariate distribution over latent features. This stochastic formulation enables the generation of informative and diverse syn-

Res	Methods	ImNet-A	ImNet-B	ImNet-C	ImNet-D	ImNet-E
128	GLaD(DC) [7]	41.8 \pm 1.7	42.1 \pm 1.2	35.8 \pm 1.4	28.0 \pm 0.8	29.3 \pm 1.3
	SLFD _{rank=10}	43.27\pm1.58	43.31\pm1.13	36.76 \pm 1.10	29.26 \pm 1.46	31.02 \pm 1.40
	SLFD _{multi}	43.21 \pm 1.55	43.20 \pm 1.13	36.81\pm1.57	29.50\pm1.09	31.25\pm1.31
256	GLaD(DC) [7]	37.4 \pm 5.5	41.5 \pm 1.2	35.7 \pm 4.0	27.9 \pm 1.0	29.3 \pm 1.2
	SLFD _{rank=10}	44.01 \pm 1.68	43.15 \pm 1.64	37.28 \pm 1.38	29.78 \pm 1.07	31.57 \pm 0.99
	SLFD _{multi}	44.16\pm1.21	43.39\pm1.44	37.40\pm1.18	30.41\pm1.16	32.05\pm1.36

Table 7: Comparison of low-rank SLFD and full-rank SLFD using a multivariate normal distribution on ImageNet.

thetic data while preserving spatial structure. Our experimental results show that SLFD consistently improves performance across a range of datasets and architectures, particularly in high-resolution settings where maintaining detail is crucial. Ablation studies confirm the flexibility and effectiveness of our approach under different generator types and covariance rank configurations. Furthermore, SLFD demonstrates strong performance on medical imaging tasks, providing both quantitative gains and visually interpretable results on histopathology data. These findings highlight the potential of SLFD as a general-purpose distillation method capable of scaling across domains and resolutions while retaining efficiency and robustness.

Acknowledgments

This work was supported by the State of Bavaria, the High-Tech Agenda (HTA) Bavaria and HPC resources provided by the Erlangen National High Performance Computing Center (NHR@FAU) of the Friedrich-Alexander-Universität Erlangen-Nürnberg (FAU) under the NHR project b180dc. NHR@FAU hardware is partially funded by the German Research Foundation (DFG) - 440719683. Support was also received from the ERC - project MIA-NORMAL 101083647. S. Cechnicka is supported by the UKRI Centre for Doctoral Training AI4Health (EP / S023283/1)

Generative AI tools were used solely to assist with word choice and to improve the language and readability of the manuscript. No content was generated or interpreted by AI beyond these purposes.

References

- [1] B. Zhao, K. R. Mopuri, H. Bilen, Dataset condensation with gradient matching, International Conference on Learning Representations (ICLR) (2020).
- [2] B. Zhao, H. Bilen, Dataset condensation with differentiable siamese augmentation, in: International Conference on Machine Learning (ICML), PMLR, 2021, pp. 12674–12685.
- [3] G. Cazenavette, T. Wang, A. Torralba, A. A. Efros, J.-Y. Zhu, Dataset distillation by matching training trajectories, in: Proceedings of the IEEE/CVF Conference on Computer Vision and Pattern Recognition, 2022, pp. 4750–4759.
- [4] B. Zhao, H. Bilen, Dataset condensation with distribution matching, Proceedings of the IEEE/CVF Winter Conference on Applications of Computer Vision (WACV) (2023).
- [5] L. Zhang, J. Zhang, B. Lei, S. Mukherjee, X. Pan, B. Zhao, C. Ding, Y. Li, D. Xu, Accelerating dataset distillation via model augmentation, in: Proceedings of the IEEE/CVF Conference on Computer Vision and Pattern Recognition (CVPR), 2023, pp. 11950–11959.
- [6] G. Zhao, G. Li, Y. Qin, Y. Yu, Improved distribution matching for dataset condensation, in: Proceedings of the IEEE/CVF Conference on Computer Vision and Pattern Recognition (CVPR), 2023, pp. 7856–7865.
- [7] G. Cazenavette, T. Wang, A. Torralba, A. A. Efros, J.-Y. Zhu, Generalizing dataset distillation via deep generative prior, in: Proceedings of the IEEE/CVF Conference on Computer Vision and Pattern Recognition (CVPR), 2023, pp. 3739–3748.
- [8] A. Sauer, K. Schwarz, A. Geiger, Stylegan-xl: Scaling stylegan to large diverse datasets, in: ACM SIGGRAPH 2022 conference proceedings, 2022, pp. 1–10.
- [9] A. Kendall, Y. Gal, What uncertainties do we need in bayesian deep learning for computer vision?, Advances in neural information processing systems 30 (2017).

- [10] M. Monteiro, L. Le Folgoc, D. Coelho de Castro, N. Pawlowski, B. Marques, K. Kamnitsas, M. van der Wilk, B. Glocker, Stochastic segmentation networks: Modelling spatially correlated aleatoric uncertainty, *Advances in neural information processing systems* 33 (2020) 12756–12767.
- [11] C. You, W. Dai, Y. Min, L. Staib, J. S. Duncan, Bootstrapping semi-supervised medical image segmentation with anatomical-aware contrastive distillation, in: *International Conference on Information Processing in Medical Imaging*, Springer, 2023, pp. 641–653.
- [12] C. Fang, Q. Wang, L. Cheng, Z. Gao, C. Pan, Z. Cao, Z. Zheng, D. Zhang, Reliable mutual distillation for medical image segmentation under imperfect annotations, *IEEE Transactions on Medical Imaging* (2023).
- [13] N. Kanwal, T. Eftestøl, F. Khoraminia, T. C. Zuiverloon, K. Engan, Vision transformers for small histological datasets learned through knowledge distillation, in: *Pacific-Asia Conference on Knowledge Discovery and Data Mining*, Springer, 2023, pp. 167–179.
- [14] S. Lei, D. Tao, A comprehensive survey to dataset distillation, *arXiv preprint arXiv:2301.05603* (2023).
- [15] R. Yu, S. Liu, X. Wang, Dataset distillation: A comprehensive review, *arXiv preprint arXiv:2301.07014* (2023).
- [16] T. Wang, J.-Y. Zhu, A. Torralba, A. A. Efros, Dataset distillation, *arXiv preprint arXiv:1811.10959* (2018).
- [17] F. P. Such, A. Rawal, J. Lehman, K. Stanley, J. Clune, Generative teaching networks: Accelerating neural architecture search by learning to generate synthetic training data, in: *International Conference on Machine Learning*, PMLR, 2020, pp. 9206–9216.
- [18] T. Nguyen, Z. Chen, J. Lee, Dataset meta-learning from kernel ridge-regression, *arXiv preprint arXiv:2011.00050* (2020).
- [19] K. Wang, B. Zhao, X. Peng, Z. Zhu, S. Yang, S. Wang, G. Huang, H. Bilen, X. Wang, Y. You, Cafe: Learning to condense dataset by aligning features, in: *Proceedings of the IEEE/CVF Conference on Computer Vision and Pattern Recognition*, 2022, pp. 12196–12205.

- [20] A. Sajedi, S. Khaki, E. Amjadian, L. Z. Liu, Y. A. Lawryshyn, K. N. Plataniotis, Datadam: Efficient dataset distillation with attention matching, in: Proceedings of the IEEE/CVF international conference on computer vision (ICCV), 2023.
- [21] S. Liu, K. Wang, X. Yang, J. Ye, X. Wang, Dataset distillation via factorization, Advances in Neural Information Processing Systems (NeurIPS) 35 (2022) 1100–1113.
- [22] J. Du, Y. Jiang, V. Y. Tan, J. T. Zhou, H. Li, Minimizing the accumulated trajectory error to improve dataset distillation, in: Proceedings of the IEEE/CVF Conference on Computer Vision and Pattern Recognition (CVPR), 2023, pp. 3749–3758.
- [23] D. Zhu, B. Lei, J. Zhang, Y. Fang, R. Zhang, Y. Xie, D. Xu, Rethinking data distillation: Do not overlook calibration, in: Proceedings of the IEEE/CVF international conference on computer vision (ICCV), 2023.
- [24] B. Zhao, H. Bilen, Synthesizing informative training samples with gan, NeurIPS 2022 Workshop on Synthetic Data for Empowering ML Research (2022).
- [25] S. Liu, X. Wang, Few-shot dataset distillation via translative pre-training, in: Proceedings of the IEEE/CVF international conference on computer vision (ICCV), 2023.
- [26] Y. Liu, J. Gu, K. Wang, Z. Zhu, W. Jiang, Y. You, Dream: Efficient dataset distillation by representative matching, in: Proceedings of the IEEE/CVF international conference on computer vision (ICCV), 2023.
- [27] A. Malinin, M. Gales, Predictive uncertainty estimation via prior networks, Advances in neural information processing systems 31 (2018).
- [28] A. Malinin, M. Gales, Reverse kl-divergence training of prior networks: Improved uncertainty and adversarial robustness, Advances in Neural Information Processing Systems 32 (2019).
- [29] M. Sensoy, L. Kaplan, M. Kandemir, Evidential deep learning to quantify classification uncertainty, Advances in neural information processing systems 31 (2018).

- [30] C. Guo, G. Pleiss, Y. Sun, K. Q. Weinberger, On calibration of modern neural networks, in: International conference on machine learning, PMLR, 2017, pp. 1321–1330.
- [31] A. G. Wilson, P. Izmailov, Bayesian deep learning and a probabilistic perspective of generalization, *Advances in neural information processing systems* 33 (2020) 4697–4708.
- [32] Z. Li, B. Kainz, Image distillation for safe data sharing in histopathology, *arXiv preprint arXiv:2406.13536* (2024).
- [33] G. Li, R. Togo, T. Ogawa, M. Haseyama, Soft-label anonymous gastric x-ray image distillation, in: 2020 IEEE International Conference on Image Processing (ICIP), IEEE, 2020, pp. 305–309.
- [34] G. Li, R. Togo, T. Ogawa, M. Haseyama, Compressed gastric image generation based on soft-label dataset distillation for medical data sharing, *Computer Methods and Programs in Biomedicine* 227 (2022) 107189.
- [35] G. Li, R. Togo, T. Ogawa, M. Haseyama, Dataset distillation for medical dataset sharing, *arXiv preprint arXiv:2209.14603* (2022).
- [36] R. Abdal, Y. Qin, P. Wonka, Image2stylegan: How to embed images into the stylegan latent space?, in: Proceedings of the IEEE/CVF international conference on computer vision (ICCV), 2019, pp. 4432–4441.
- [37] J. Deng, W. Dong, R. Socher, L.-J. Li, K. Li, L. Fei-Fei, Imagenet: A large-scale hierarchical image database, in: 2009 IEEE conference on computer vision and pattern recognition, Ieee, 2009, pp. 248–255.
- [38] A. Krizhevsky, G. Hinton, et al., Learning multiple layers of features from tiny images (2009).
- [39] J. Yang, R. Shi, D. Wei, Z. Liu, L. Zhao, B. Ke, H. Pfister, B. Ni, Medmnist v2-a large-scale lightweight benchmark for 2d and 3d biomedical image classification, *Scientific Data* 10 (1) (2023) 41.
- [40] F. Bao, S. Nie, K. Xue, Y. Cao, C. Li, H. Su, J. Zhu, All are worth words: A vit backbone for diffusion models, in: Proceedings of the IEEE/CVF Conference on Computer Vision and Pattern Recognition (CVPR), 2023, pp. 22669–22679.

- [41] A. Dosovitskiy, L. Beyer, A. Kolesnikov, D. Weissenborn, X. Zhai, T. Unterthiner, M. Dehghani, M. Minderer, G. Heigold, S. Gelly, et al., An image is worth 16x16 words: Transformers for image recognition at scale. arxiv 2020, arXiv preprint arXiv:2010.11929 (2010).